Available online at www.sciencedirect.com
SCIENCE DIRECT®
Journal of Solid State Chemistry 178 (2005) 3159–3168
JOURNAL OF SOLID STATE CHEMISTRY
www.elsevier.com/locate/jssc

Compositionally modulated Fermi surfaces, structured diffuse scattering and ternary derivatives of 1T-TaS_2

Ray Leslie Withers[a,*], Carlos Otero-Diaz[b,c], Adrian Gómez-Herrero[b], A.R. Landa-Canovas[d], Albert Prodan[e], Herman J.P. van Midden[e], Lasse Norén[a]

[a]*Research School of Chemistry, Australian National University, Canberra, ACT 0200, Australia*
[b]*Dpto. Química Inorgánica, Facultad de Ciencias Químicas, Universidad Complutense, E-28040 Madrid, Spain*
[c]*Centro de Microscopía, Universidad Complutense, E-28040 Madrid, Spain*
[d]*Insto. Ciencia de Materiales, CSIC, E-28049 Madrid, Spain*
[e]*Jožef Stefan Institute, Jamova 39, SI-1000 Ljubljana, Slovenia*

Received 20 June 2005; received in revised form 25 July 2005; accepted 28 July 2005
Available online 26 August 2005

Abstract

Ternary derivatives of 1T-TaS_2 have been synthesized and the variation in the highly structured diffuse intensity distributions characteristic of such materials carefully monitored to investigate the effect that such substitution has upon the band structures and Fermi surfaces (FSs) of the materials. Removal of *d* electrons via the replacement of Ta ions with lower valent transition metal ions leads to a systematic increase in the radii of the characteristic structured diffuse intensity distribution. Extended Hückel tight binding calculations of the FSs of the doped samples are carried out and used to predict possible nesting wave-vectors. The results are in reasonably good agreement with the radii of the experimentally observed diffuse intensity distributions.

Keywords: Ternary derivatives of 1T-TaS_2; Structured diffuse scattering; Effect of doping upon; Fermi surface; Effect of doping upon; Tight binding calculations

1. Introduction

Layered transition metal chalcogenides have long been of interest for their low dimensional electronic band structures, susceptibility to displacive structural phase transitions and temperature-dependent metal to insulator phase transitions [1–12]. The so-called 1T polymorph of TaS_2, for example, undergoes at least three such phase transitions on both heating and cooling [1–4,8,9].

All these phases can be described as modulated variants of the same underlying trigonal $P\bar{3}m1$ parent structure in which a layer of Ta atoms (each in octahedral co-ordination) is sandwiched between a double layer of S atoms (see Fig. 1). The bonding within each such three-atom layer sandwich is strongly covalent, with only relatively weak van der Waals bonding holding the individual sandwiches together. Each S atom is covalently bonded to 3 neighbouring Ta atoms thus each Ta–S bond formally uses $\frac{2}{3}$ of a Ta *d* electron. There are 6 such Ta–S bonds for each Ta atom. Thus Ta uses 4 out of its 5 *d* electrons in this covalent bonding. The remaining fifth *d* electron delocalizes within the (001) planes of Ta atoms to form an essentially two-dimensional metal with a largely cylindrical free Fermi surface [7]. A major interest in this and related compounds stems from the fact that this free Fermi surface causes coupled charge density wave/periodic lattice distortion (CDW/PLD) instabilities whose periodicity is directly related to the radius of the Fermi surface [3,7].

*Corresponding author. Fax: +61 2 6125 0750.
E-mail address: withers@rsc.anu.edu.au (R.L. Withers).

0022-4596/$ - see front matter © 2005 Elsevier Inc. All rights reserved.
doi:10.1016/j.jssc.2005.07.032

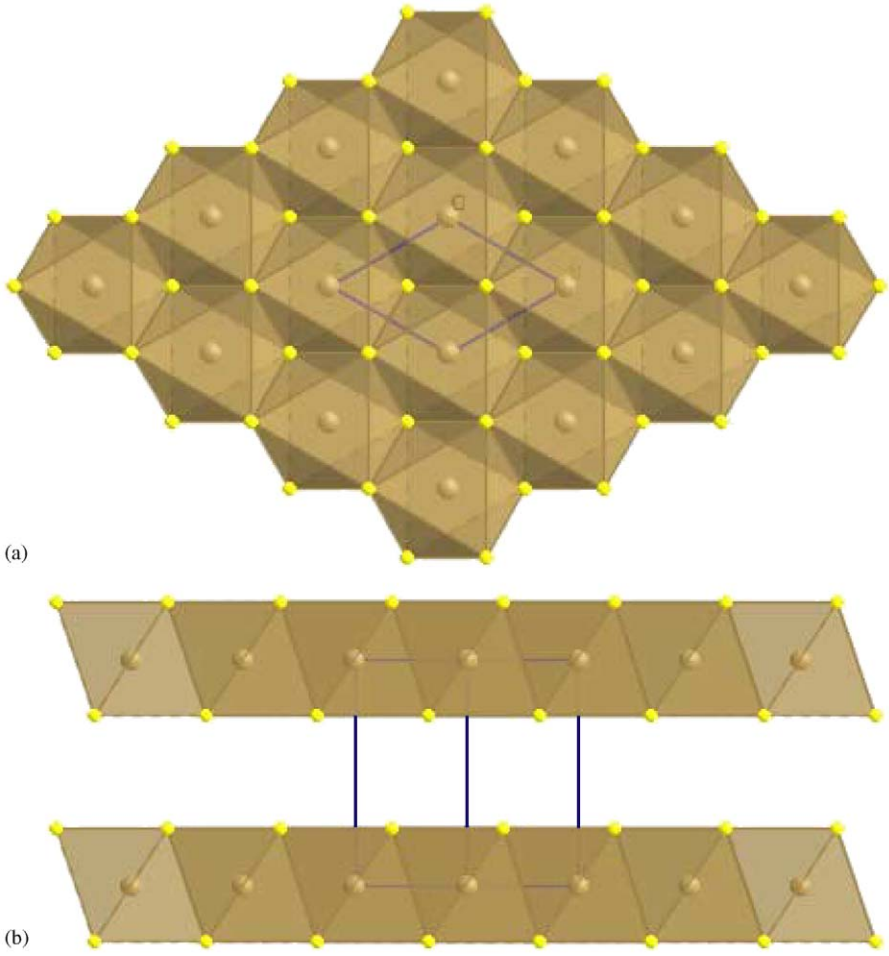

Fig. 1. The underlying trigonal $P\bar{3}m1$ parent structure of the 1T polymorph of TaS_2 in projection along [001] in (a) and $\langle 110 \rangle$ in (b).

This Fermi surface induced instability manifests itself in the form of characteristic, longitudinally 'polarized' cylinders of diffuse intensity of radius $\sim 0.72a^*$ surrounding each strong Bragg reflection of the underlying parent structure in the highest temperature (above $\sim$543 K) so-called $1T_0$ polymorph of TaS_2 [8,10]. The same structured diffuse distribution also exists within the $1T_1$ polymorph from 543 K down to 350 K [2,5,10], although to a lesser extent given the co-existence of sharp incommensurate satellite reflections—see e.g. Fig. 9 of [5]. Note that the highest temperature $1T_0$ polymorph of TaS_2 (along with its associated diffuse intensity distribution) can be stabilized down to room temperature via light doping of TaS_2 ($\sim$2–3%) with VS_2, as shown in Fig. 2 (see also [10]). That this characteristic diffuse intensity distribution is largely displacive in origin is clear from the azimuthal intensity variation of the diffuse distribution [10]. The structured diffuse scattering arises from static, short-range ordered, CDW induced metal–metal bonding within the (001) Ta atom planes of the underlying parent structure (and associated structural relaxation also involving the S ions—see e.g. [11]).

On cooling from the $1T_0$ state above 543 K, TaS_2 undergoes a series of polymorphic phase transitions all associated with sharp (usually incommensurate) satellite reflections condensing out on to the higher temperature $1T_0$-type diffuse distribution—compare, for example, Fig. 9 of [5] with Fig. 2 [2–4,8–11]. In this contribution, we will concentrate primarily on the high temperature diffuse distribution itself as this is most directly related to the largely two-dimensional band structure and free Fermi surface and because it can be modified by replacement of the Ta atoms with other transition metal atoms with a different *d* electron count [12]. By replacing Ta atoms with other transition metals with differing numbers of *d* electrons such as, for example, Ti^{4+}, Zr^{4+}, Hf^{4+} or Cr^{3+} it should be possible to modify this free Fermi surface [11] and hence the radius of the diffuse cylinders observed in electron diffraction (see Fig. 2).

In this contribution we have investigated the effect of such replacement upon the diffuse intensity distributions

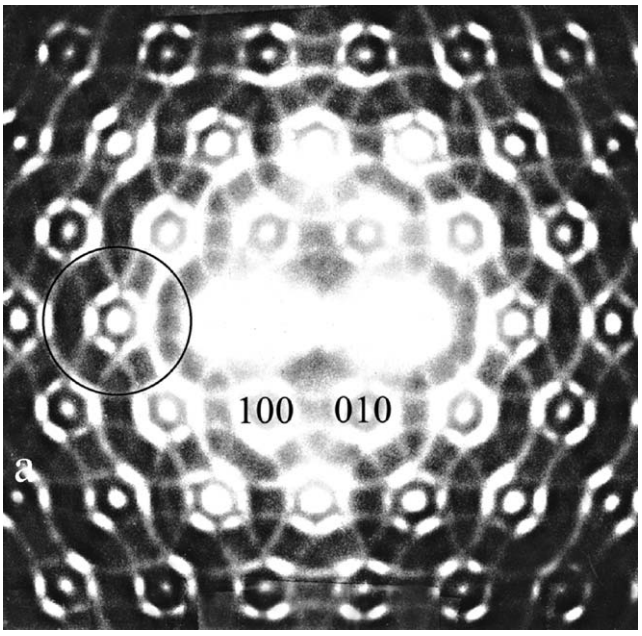

Fig. 2. A close to [001] zone axis EDP of CDW modulated 1T$_0$-$Ta_{1-x}V_xS_2$ ($x\sim0.02$) (first reported in [10]). Notice the diffuse circles of radius $0.72a^*$ surrounding each Bragg reflection of the underlying $P\bar{3}m1$ parent structure. One such diffuse circle has been highlighted.

characteristic of the 1T-TaS_2 CDW/PLD system. Two compositions doped with substantial but differing amounts of transition metals have been synthesized and investigated, 1T-$Ta_{0.50}V_{0.375}Cr_{0.125}S_2$ and 1T-$Ta_{0.44}Ti_{0.29}Cr_{0.26}S_2$ (see below). Their behaviour will be compared with that of 1T-TaS_2 itself, both experimentally and theoretically via extended Hückel tight binding (EHTB) calculations.

2. Experimental

2.1. Synthesis

Doped $Ta_{1-x}M_xS_2$, $M = V + Cr$ and $Ti + Cr$, samples were prepared by heating the appropriate amounts of elemental Ta, V, Ti, Cr and S elements (a slight excess of S (10%) was used in order to facilitate reaction). Ground mixtures were heated in vacuum-sealed silica tubes, 40 cm in length and with an internal diameter of 11 mm. The end of the tube containing the starting materials was initially kept outside the furnace and only slowly inserted into the furnace over a 6-day period (in order to avoid excessive S over-pressure). The temperature in the furnace was increased very slowly up to 1223 K over the same period of 6 days and then held at 1223 K for 15 days. After 15 days at this temperature the sample was cooled down by switching off the furnace. After gentle grinding, the resultant blackish-grey microcrystalline powder was heated again in the presence of I_2(s) (4 mg/cm^3) in an evacuated silica tube for a further 28 days at 1223 K prior to final slow cooling to room temperature.

2.2. Transmission electron microscopy

Transmission electron microscope (TEM) analysis was carried out on Philips EM 430 and CM 200 FEG TEMs as well as on a JEOL JEM 3000 F TEM on crushed grains of the samples dispersed onto holey carbon-coated copper grids.

2.3. Scanning electron microscopy

The size and morphology of the samples were investigated on a JSM 6335 F scanning electron microscope (SEM).

2.4. X-ray diffraction

The X-ray powder diffraction (XRD) patterns were collected using a Guinier–Hägg camera with Cu$K\alpha_1$ radiation. Silicon (NBS no. 640) was used as an internal standard to accurately determine unit cell parameters, refined using the ''Unitcell'' software package [13].

3. Results

3.1. EDS analysis

Energy dispersive spectroscopy (EDS) in the TEM was performed to check homogeneity and to verify the compositions of the synthesized compounds. The composition of the $M = V + Cr$ doped phase was determined by semi-quantitative EDS analysis (from 5 crystals analysed at two separate points, i.e. 10 separate analyses overall) to have stoichiometry $Ta_{0.50}V_{0.375}Cr_{0.125}S_2$. The composition of the second doped TaS_2 phase was likewise determined by semi-quantitative EDS analysis to have stoichiometry $Ta_{0.44}Ti_{0.29}Cr_{0.26}S_2$.

3.2. Scanning electron microscopy

Both phases exhibited a rather intriguing sample morphology in the form of thin plates with a completely round shape, like biscuits with an up to $\sim$2 mm diameter, as can be seen in the SEM images of Fig. 3. The morphology of the round plates is presumably controlled by the development of the (001) faces of the trigonal unit cells. That the crystals grow much more readily perpendicular to the c-axis than along it is not surprising. That they should take a round, rather than a hexagonal or trigonal, shape is rather

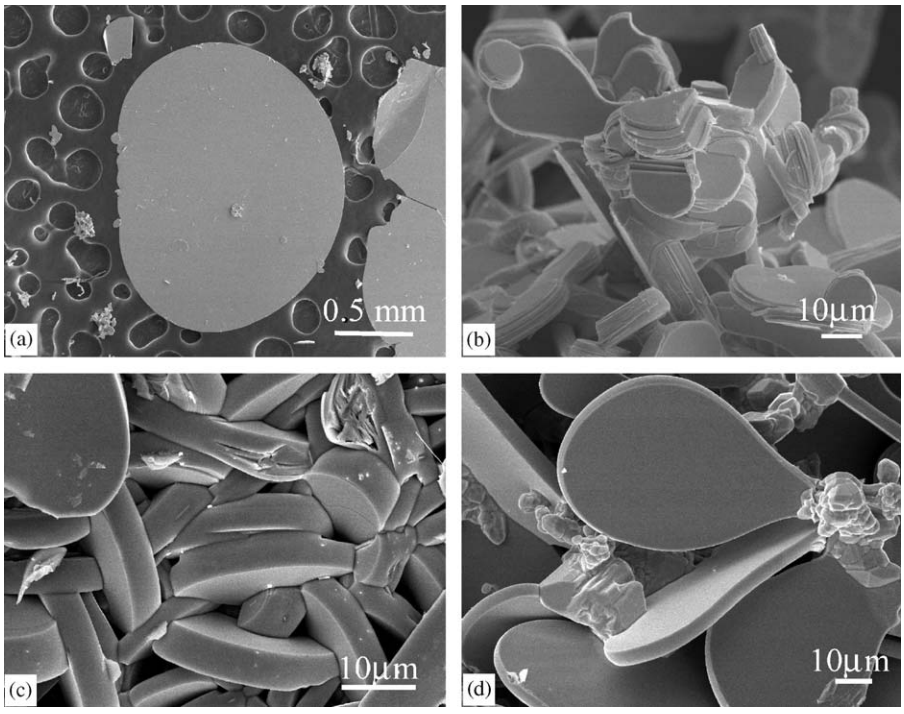

Fig. 3. SEM micrographs taken at 15 kV of the biscuit shaped crystals of (a,b) 1T-$Ta_{0.50}V_{0.375}Cr_{0.125}S_2$ and (c,d) 1T-$Ta_{0.44}Ti_{0.29}Cr_{0.26}S_2$.

more surprising given the $P\bar{3}m1$ average structure space group symmetry.

3.3. X-ray diffraction

Guinier XRD patterns of both phases confirmed that they were indeed ternary derivatives of 1T-TaS_2 with trigonal cell dimensions closely related to those of TaS_2 itself (see Table 1). In the case of $Ta_{0.50}V_{0.375}Cr_{0.125}S_2$, the refined cell dimensions were $a = b = 3.3619(4)$ Å, $c = 5.835(2)$ Å, while in the case of $Ta_{0.44}Ti_{0.29}Cr_{0.26}S_2$, $a = b = 3.3899(1)$ Å, $c = 5.793(1)$ Å. The reported average structure unit cell dimensions of TaS_2 itself at room temperature are $a = b = 3.3649(1)$, $c = 5.8971(2)$ Å [11]. (Note that pure TaS_2 is in the modulated $1T_2$ state at room temperature rather than the $1T_0$ state characteristic of the two ternary derivative phases—see e.g. [11]). The primary effect of the ternary alloying appears to be a slight (~1–2%) reduction in the c parameter which presumably indicates slightly increased S–S inter-layer interactions across the van der Waal's gap. The a parameter of $Ta_{0.50}V_{0.375}Cr_{0.125}S_2$ is virtually unchanged while the a parameter of $Ta_{0.44}Ti_{0.29}Cr_{0.26}S_2$ increases slightly (~0.7%).

Table 1
Unit cell dimensions and reciprocal space radii of the diffuse cylinders characteristic of TaS_2 and the doped TaS_2 samples

	TaS_2	$Ta_{0.50}V_{0.375}Cr_{0.125}S_2$	$Ta_{0.44}Ti_{0.29}Cr_{0.26}S_2$
Circle radii	$0.72a^*$	$0.758a^*$	$0.825a^*$
a (Å)	3.3649(1)	3.3619(4)	3.3899(1)
c (Å)	5.8971(2)	5.835(2)	5.793(1)

The room temperature unit cell dimensions for TaS_2 quoted are taken from Ref. [11].

3.4. Electron microscopy

Lattice imaging of both doped compounds confirmed the expected underlying $P\bar{3}m1$ average structure. Fig. 4a for example, shows an [001] zone axis HREM image of the $Ta_{0.50}V_{0.375}Cr_{0.125}S_2$ sample from a thin crystal region. The fast Fourier transform (FFT) diffraction pattern of this crystal region, shown as the inset to this image, shows no clear evidence for structured diffuse scattering. The corresponding filtered image is shown in Fig. 4b. The projected hexagonal parent structure unit cell is clearly apparent in both images. There is, however, no indication of additional contrast arising from short-range ordered metal–metal bonding and associated structural relaxation in these exact on-axis images. Likewise exact [001] zone axis electron diffraction patterns (EDPs) (see Fig. 4f) also show no evidence for structured diffuse scattering.

HREM images taken slightly off-axis, however, do show mottled contrast presumably indicative of local short-range order (see Fig. 4c). The FFT diffraction pattern of this image (inset into Fig. 4c) also shows evidence for structured diffuse scattering as does the

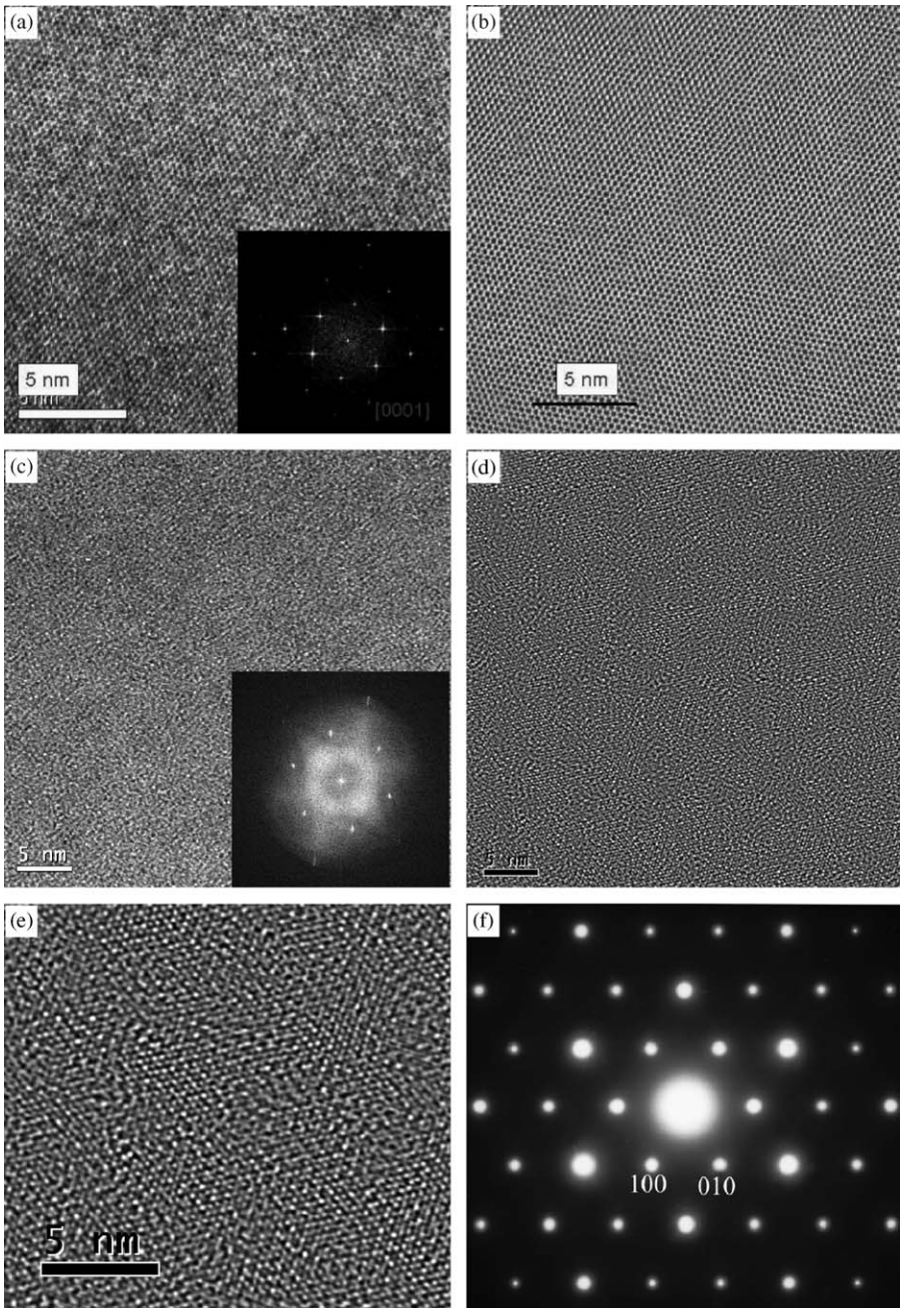

Fig. 4. (a) An [001] zone axis HREM image of the $Ta_{0.50}V_{0.375}Cr_{0.125}S_2$ sample from a thin crystal region. The FFT diffraction pattern of this crystal region is shown as an inset in (a) and the corresponding filtered image in (b). The corresponding [001] zone axis EDP is shown in (f). A HREM image taken slightly off-axis is shown in (c) and shows mottled contrast indicative of local short-range order. The FFT diffraction pattern of this image is shown as an inset in (c). It also shows evidence for structured diffuse scattering. The corresponding Fourier filtered image is shown in (d) and an enlargement thereof in (e).

corresponding Fourier filtered image shown in Fig. 4d and the enlargement thereof shown in Fig. 4e. The interpretation of such off-axis images, however, is far from straightforward. Santiago et al. [14], for example, have recently shown that rotation can have a dramatic effect on apparent domain-like contrast in slightly off-axis HREM images of twisted MoS_2 nanotubes. We do not therefore claim that the contrast apparent in Fig. 4e can be directly interpreted in terms of local domain size or such like.

While no diffuse distribution is observed in [001] zone axis EDPs (see e.g. Fig. 4f), on tilting slightly away from the exact [001] zone axis orientation a highly structured, quite reproducible and largely tilt insensitive diffuse intensity distribution immediately becomes apparent in both cases (see Fig. 5). Fig. 5a shows a close to [001]

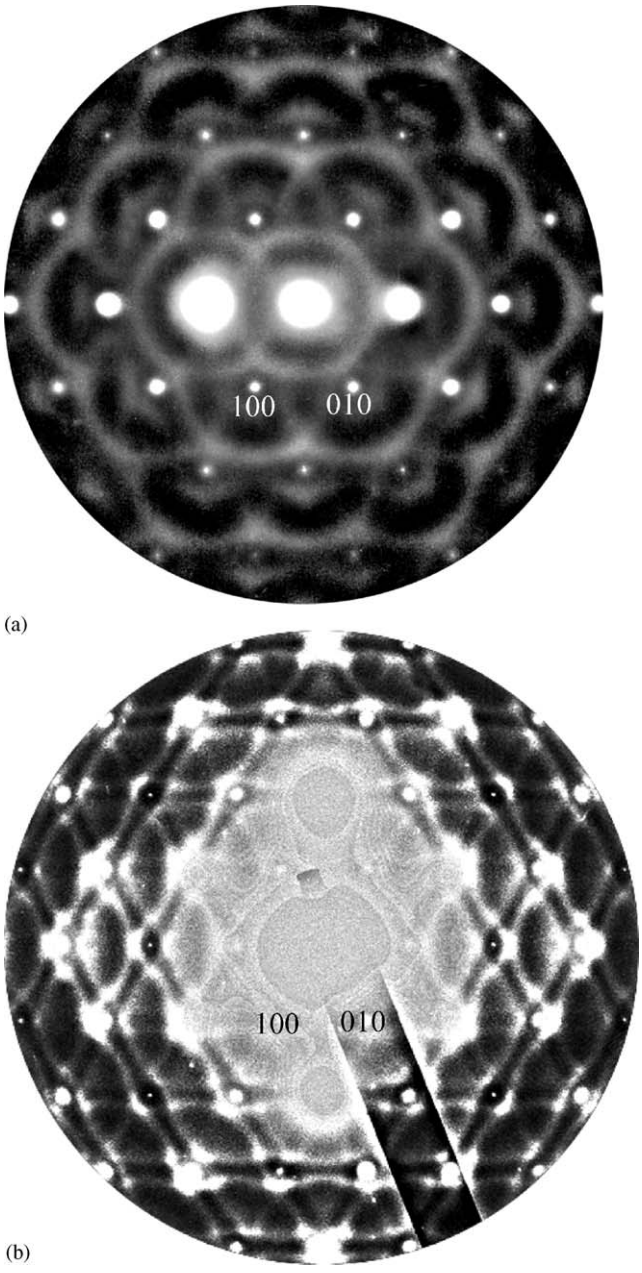

Fig. 5. Close to [001] zone axis EDPs of (a) 1T-$Ta_{0.50}V_{0.375}Cr_{0.125}S_2$ and (b) 1T-$Ta_{0.44}Ti_{0.29}Cr_{0.26}S_2$.

zone axis EDP of the $Ta_{0.50}V_{0.375}Cr_{0.125}S_2$ sample while Fig. 5b shows a close to [001] zone axis EDP of the $Ta_{0.44}Ti_{0.29}Cr_{0.26}S_2$ sample. Both EDPs are clearly closely related to the equivalent close to [001] zone axis EDP of the lightly VS_2-doped TaS_2 sample shown in Fig. 2. Note that the radii of the characteristic diffuse circles apparent in each EDP has clearly altered for the heavily substituted samples. In the case of 1T-$Ta_{0.50}V_{0.375}Cr_{0.125}S_2$, the diffuse cylinders are characterized by a reciprocal space radius of $\sim 0.76a^*$ (see Table 1) whereas, in the case of 1T-$Ta_{0.44}Ti_{0.29}Cr_{0.26}S_2$, electron diffraction found a rather larger radius more like ~ 0.82–$0.83a^*$. No evidence was found for any ordering of the substituting ions in either case, i.e. the average structure cell remains the same as for TaS_2 itself. We therefore presume the primary effect of the substituting ions is simply to modify the free Fermi surface.

Both of the ternary samples were also cooled in a liquid nitrogen sample holder to see if any satellite reflections might condense out onto the diffuse distribution upon cooling as occurs in the case of TaS_2 itself (cf., for example, Fig. 9 of [5] with Fig. 2). TEM observations in the cooling specimen holder (at liquid nitrogen temperature, i.e. 77 K), however, did not reveal any change in the diffuse intensity distributions in either case.

4. Theoretical interpretation

In order to gain insight into the Fermi surface nesting responsible for the observed diffraction phenomena and the effect that transition metal substitution might have upon it we have also undertaken calculations within the EHTB approximation [15–17]. This method uses (semi)-empirical tight-binding Hamiltonians that employ linear combinations of atomic orbitals. It has successfully been used to describe the electronic properties of both periodic and non-periodic systems [18–22] as well as CDW phenomena in related transition-metal chalcogenides (see e.g. [23]).

Because of its simplified approach, EHTB calculations scale linearly with the number of atoms and are

Table 2
Extended Huckel parameters from the CEASAR package [16]

Orbital		H_{ii} (eV)	Exponents	
			$\zeta 1$[a]	$\zeta 2$[a]
Ta	6*s*	−10.1	2.28	
	6*p*	−6.86	2.241	
	5*d*	−12.1	4.762 (0.6815)	1.938 (0.5589)
S	3*s*	−20.0	2.122	
	3*p*	−13.3	1.827	
Cr	4*s*	−8.66	1.7	
	4*p*	−5.24	1.7	
	3*d*	−11.22	4.95 (0.506)	1.8 (0.675)
V	4*s*	−8.81	1.3	
	4*p*	−5.52	1.3	
	3*d*	−11.0	4.75 (0.4755)	1.7 (0.7052)
Ti*	4*s*	−8.97	1.6	
	4*p*	−5.44	1.6	
	3*d*	−10.81	4.321 (0.46805)	1.673 (0.68608)

Ti parameters from [17].
[a]Exponents and coefficients (in parentheses) in a double-ζ expansion of the metal *d* orbitals.

able to handle large systems, up to a few hundred atoms, on inexpensive computational systems. This makes it ideal to study the influence of small structural and compositional changes on electronic properties. In this work we have used the CEASAR package [17] to calculate dispersion curves (DCs), (partial) density of states (P)(DOSs) and Fermi surfaces (FSs) in order to determine possible CDW nesting conditions.

In order to assess the validity of the method, the electronic properties of the pure 1T-TaS_2 system were first calculated (assuming the parent $P\bar{3}m1$, $a_0 \times a_0 \times c_0$ hexagonal unit cell). Table 2 lists the potential parameters used. The electronic properties were calculated by sampling 2541 points in **k**-space (21 points along the **a*** direction and 11 points along the **b*** and **c*** directions). The resultant calculated FS of TaS_2, shown in Fig. 6c, is in good agreement with the FS previously reported by Inglesfield [7].

In order to investigate the doped systems, the parent unit cell has to be enlarged appropriately in order to enable the overall composition to be varied in accordance with the nominal compositions studied. Calculation of electronic properties in the case of doped crystals is not a straightforward problem. Disorder cannot be introduced by simply putting different atoms with corresponding weights into the same crystallographic positions. A proper choice of the enlarged cell is crucial. A number of distinct possible ways of enlarging the parent unit cell were considered. Since we were mainly interested in the FS structure in the **a***–**b*** plane and the compounds considered are known to be quasi two-dimensional, the enlargement of the parent unit cell was chosen to be along the crystallographic **c**-direction only. In this way larger overlapping of higher-order Brillouin zones (BZs) perpendicular to **c*** in the reciprocal space could be avoided.

An enlarged ($a_0 \times a_0 \times 16c_0$) hexagonal cell was chosen to approximate the doped systems studied. Thus, instead of simulating $Ta_{0.5}V_{0.375}Cr_{0.125}S_2$ and $Ta_{0.44}Ti_{0.29}Cr_{0.26}S_2$ within the parent unit cell, calculations were performed for $Ta_8V_6Cr_2S_{32}$ and $Ta_7Ti_5Cr_4S_{32}$ within an enlarged ($a_0 \times a_0 \times 16c_0$) cell. A total of 21 points along the **a***, 11 points along the **b*** and 3 points along the **c*** direction were sampled in ***k***-space for the

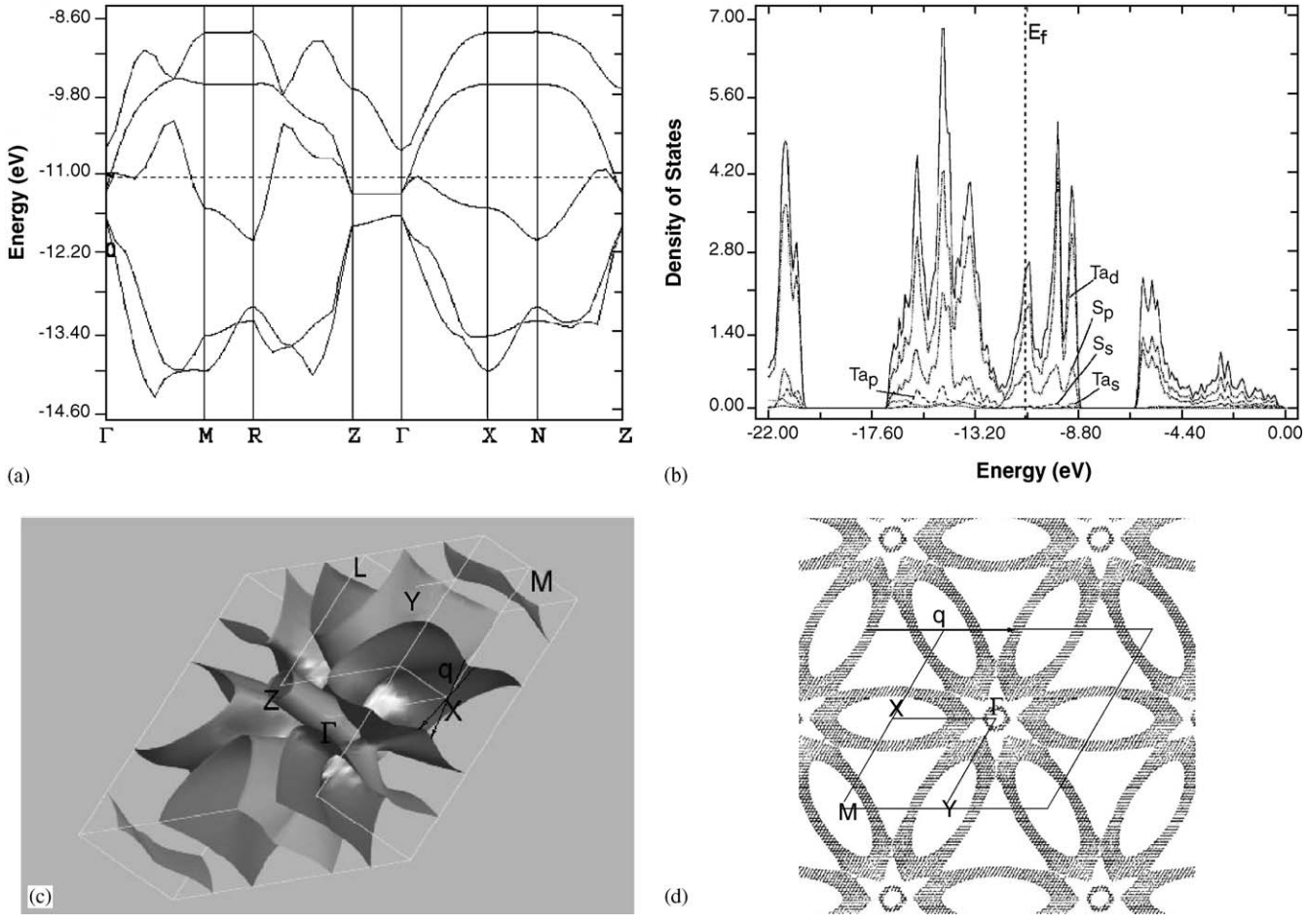

Fig. 6. DCs (a), partial DOSs spectra (b), the Fermi surface within the basic reciprocal unit cell (c) and its projection along the **c*** direction (d) of TaS_2. The arrows in (c) shows the possible nesting direction (***q***), corresponding to the experimentally determined $q = 0.71a^*$ (calculation performed within the $a_0 \times a_0 \times c_0$ unit cell).

enlarged cell. While the composition of the first of these two compounds corresponds exactly to its nominal value, the second represents a close approximant only.

Since the chosen enlargement of the parent unit cell necessarily introduces additional order into the system, the influence on the electronic properties were checked by performing DC and (P)DOS calculations for a series of different cells. The results confirmed the expectation that ordering along the **c**-direction has a negligible influence on the FS shape in the **a***–**b*** plane. Thus, the calculated FSs for TaS_2 and $Ta_{16}S_{32}$ are practically identical in projection along **c***.

4.1. Calculation results

In Fig. 6, (a) DCs, (b) PDOS spectra and (c) the corresponding FS for TaS_2 are shown. The FS shown in Fig. 6c reveals a typical quasi-two-dimensional character. Intriguingly, however, the flatter areas of the FS are not ideally straight, i.e. the areas of the FS responsible for nesting are not exactly perpendicular to the S–Ta–S layers. Thus, it is perhaps not surprising that the first set of sharp incommensurate satellite reflections that condense out onto the higher temperature $1T_0$-type diffuse distribution at the $1T_0$–$1T_1$ phase transition (see e.g. [10]) have a non-zero **c*** component. It may also help explain why the crystals have to be tilted slightly out of the exact [001] zone axis orientation in order to observe the diffuse rings (see Fig. 5). Possible nesting wave-vectors, connecting parallel parts of the FS, are also shown in Fig. 6c. The basal plane magnitude, q, of these nesting wave-vectors is given by $q = 0.71a^*$. In the projection of the FS along the **c*** direction shown in Fig. 6d the same nesting wave-vector magnitude is again indicated. Its magnitude ($q = 0.71a^*$) is in rather good agreement with the experimentally determined value of $q = 0.72a^*$ (see Table 1).

Via the same process, nesting wave-vectors can also be deduced for both $Ta_8V_6Cr_2S_{32}$ (see Fig. 7) and $Ta_7Ti_5Cr_4S_{32}$ (see Fig. 8). The corresponding FS

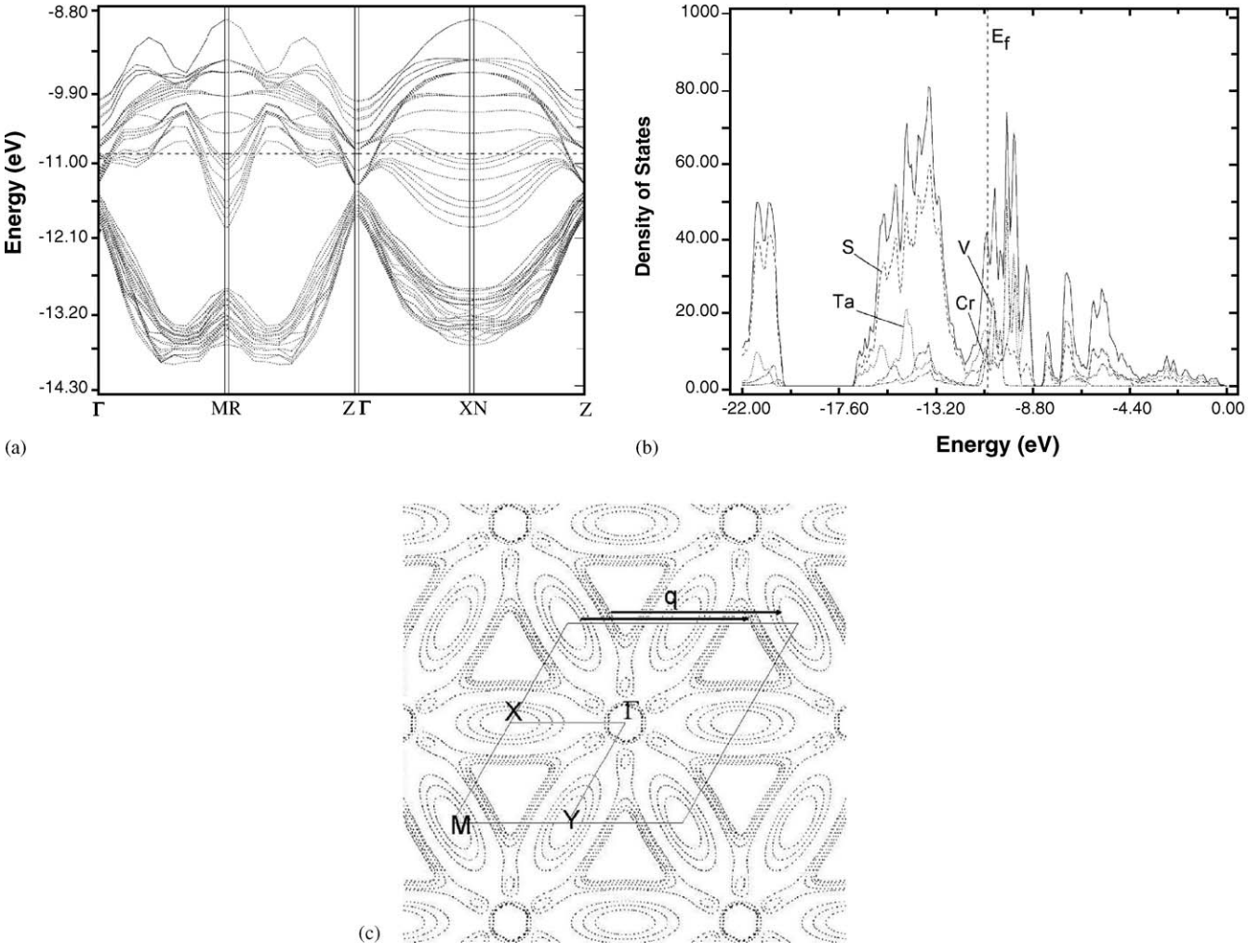

Fig. 7. DCs (a), partial DOSs spectra (b) and the projection of the Fermi surface along the **c*** direction (c) of $Ta_8V_6Cr_2S_{32}$. The arrows in (c) show the projection of the possible nesting direction with $q = 0.74a^*$ (calculation performed within the $a_0 \times a_0 \times 16c_0$ unit cell). The two arrows in (c) connect different nested portions of the calculated Fermi surface.

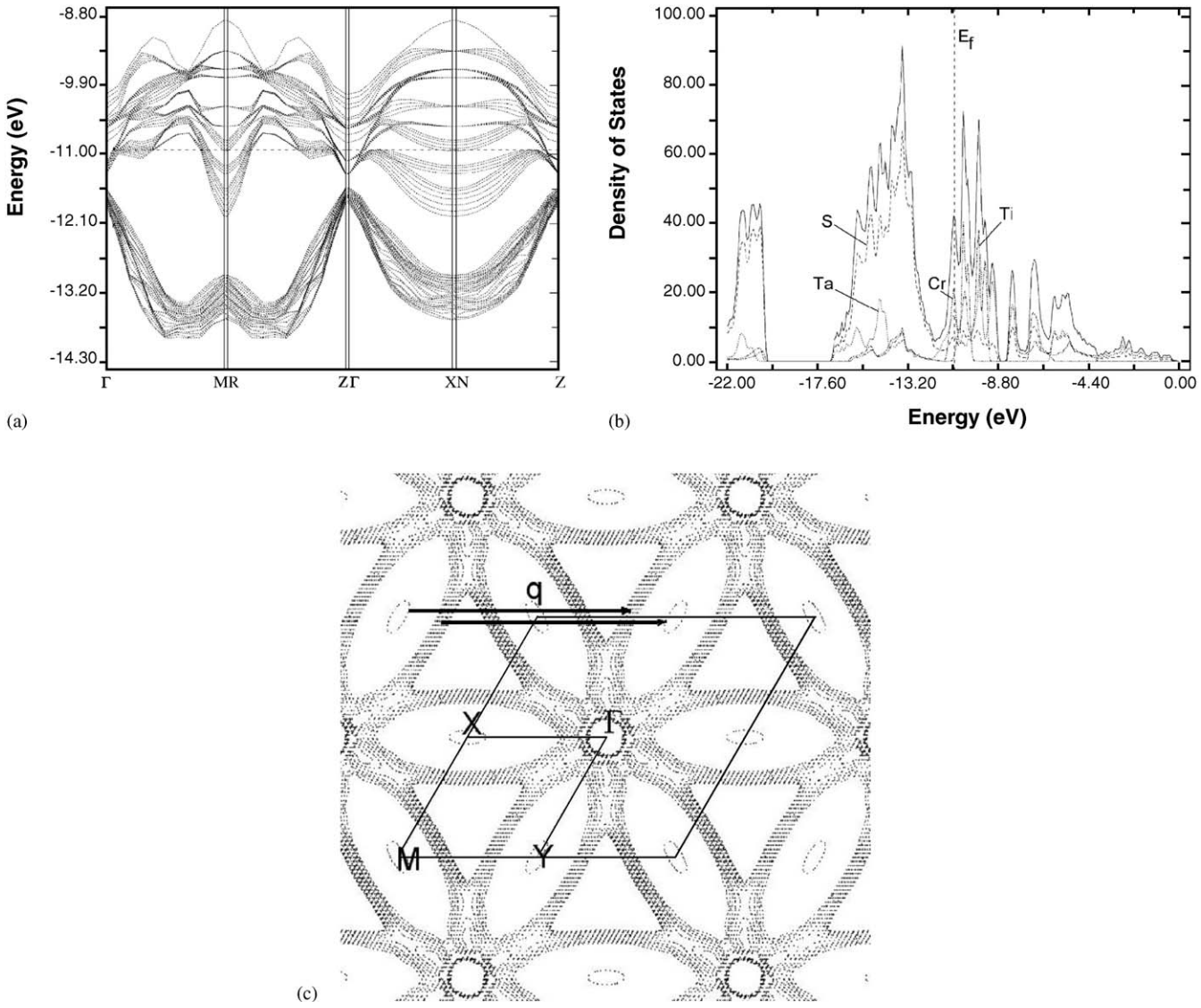

Fig. 8. DCs (a), partial DOSs spectra (b) and the projection of the Fermi surface along the **c*** direction (c) of $Ta_7Ti_5Cr_4S_{32}$. The arrow shows the possible nesting direction, corresponding to $q = 0.80a^*$ (calculation performed within the $a_0 \times a_0 \times 16c_0$ unit cell). The two arrows in (c) connect different nested portions of the calculated Fermi surface.

projections along **c*** for the latter compounds are found to retain the general shape of the FS of TaS_2 (and $Ta_{16}S_{32}$) (cf. Figs. 6d, 7c and 8c). The modulation q-vectors which span equivalent parts of the FS to those in pure TaS_2 and support nesting are indicated in Figs. 7c and 8c. The magnitude of these nesting wave-vectors ($0.74a^*$ and $0.80a^*$) are in reasonably good accord with the experimental values given in Table 1, i.e. $q = 0.76a^*$ and $0.83a^*$, respectively. There are a few potential reasons for the small discrepancies between the calculated and experimental values. Firstly, the tabulated parameters for Ti used in the EHTB calculations were taken from a different source to those listed in the CESAR package (see Table 2). Secondly, the discrepancy in the exact composition of the approximate as compared to the nominal composition may cause a slight variation either in the height of the Fermi level E_f or in the dispersion of the contours in the case of the $Ta_{0.44}Ti_{0.29}Cr_{0.26}S_2$ compound. Overall, however, the agreement between experiment and theory is remarkably good.

5. Discussion

These results can also be rationalized with reference to the results of di Salvo et al. [12] where it was shown that the radii of the diffuse cylinders did not change if Ta is replaced by ions such as V^{5+} or Nb^{5+} (where $5d$ electrons are also donated to the free FS) but increased

significantly (the radius we have defined is given by 1−the radius given in Fig. 12 of [12]) if Ta is replaced by significant amounts of Ti^{4+} which only donates 4*d* electrons to the free Fermi surface. If we make the assumption that V is in the 5+ valence state, Ti in the 4+ valence state and Cr in the 3+ valence state, then 1T-$Ta_{0.50}V_{0.375}Cr_{0.125}S_2$ corresponds to the removal of ~0.25 electrons and 1T-$Ta_{0.44}Ti_{0.29}Cr_{0.26}S_2$ to the removal of ~0.81 electrons relative to 1T-TaS_2 itself. From Fig. 12 of di Salvo et al. [12] we might therefore expect a measured diffuse radius of $\sim 0.75a^*$ in the former case and $\sim 0.86a^*$. While the agreement with experimental observation is by no means perfect, the general increase in radius with increasing removal of *d* electrons is consistent with the previously published results of di Salvo et al. [12]. It is also in agreement with the results of the EHTB calculations (see Figs. 6–8).

Acknowledgments

RLW acknowledges the Australian Research Council (ARC) for financial support in the form of an ARC Discovery Grant as well as the ANU Electron Microscope Unit for access to equipment. CO-D and AP thank the Research School of Chemistry of the Australian National University for Visiting Fellowships.

References

[1] A.H. Thomson, F.R. Gamble, J.F. Revelli, Solid State Commun. 9 (1971) 981–985.
[2] J. van Landuyt, G. van Tendeloo, S. Amelinckx, Phys. Status Solidi A 26 (1974) 359–370.
[3] J.A. Wilson, F.J. di Salvo, S. Mahajan, Adv. Phys. 24 (1975) 117–201; also reprinted as Adv. Phys. 50 (2001) 1171–1248.
[4] C.B. Scruby, P.M. Williams, G.S. Parry, Philos. Mag. 31 (1975) 255–265.
[5] R.L. Withers, J.A. Wilson, J. Phys. C 19 (1986) 4809–4845.
[6] P.M. Williams, in: F. Levy (Ed.), Crystallography and Crystal Chemistry of Materials with Layered Structures, vol. 2, Reidel, Dordrecht, 1976, pp. 51–92.
[7] J.E. Inglesfield, J. Phys. C 13 (1980) 17–36.
[8] S.C. Bayliss, A. Clarke, W.L. Liang, J. Phys. C 16 (1983) L831–L834.
[9] R.L. Withers, J.W. Steeds, J. Phys. C 20 (1987) 4019–4041.
[10] R.L. Withers, T.R. Welberry, J. Phys. C 20 (1987) 5975–5982.
[11] A. Spijkerman, J.L. de Boer, A. Meetsma, G.A. Wiegers, S. van Smaalen, Phys. Rev. B 56 (1997) 13757–13767.
[12] F.J. di Salvo, J.A. Wilson, B.G. Bagley, J.V. Waszczak, Phys. Rev. B 12 (1975) 2220–2235.
[13] B. Nölang, Inst. Materialkemi, Ångströmlaboratoriet, Box 538, Uppsala, Sweden.
[14] P. Santiago, J.A. Ascencio, D. Mendoza, M. Pérez-Alvarez, A. Espinosa, C. Reza-Sangermán, P. Schabes-Retchkiman, G.A. Camacho-Bragado, M. José-Yacamán, Appl. Phys. A 78 (2004) 513–518.
[15] M.-H. Whangbo, R. Hoffmann, J. Am. Chem. Soc. 100 (1978) 6093–6098.
[16] M.-H. Whangbo, R. Hoffmann, R.B. Woodward, Proc. Roy. Soc. London Ser. A 366 (1979) 23–36.
[17] J. Ren, W. Liang, M.-H. Whangbo, CEASAR Program, PrimeColour Software Inc., Cary, NC, 1998.
[18] (a) T.R. Ward, R. Hoffmann, M. Shelef, Surf. Sci. 289 (1993) 85–99;
(b) D.L. Vuckovic, S.A. Jansen, R. Hoffmann, Langmuir 6 (1990) 732–746;
(c) M.C. Zonnevylle, R. Hoffmann, Langmuir 3 (1987) 452–459.
[19] (a) Z.X. Yang, K. Zhang, X. Xie, Surf. Sci. 382 (1997) 100–106;
(b) H. Fu, L. Ye, K. Zhang, X. Xie, Surf. Sci. 341 (1995) 273–281;
(c) I. Efremenko, M. Sheintuch, Surf. Sci. 414 (1998) 148–158;
(d) P. Sonnet, L. Stauffer, S. Saintenoy, C. Piffi, P. Wetzel, G. Gewinner, C. Minot, Phys. Rev. B 56 (1997) 15171–15179;
(e) C. Noce, M. Cuoco, Phys. Rev. B 59 (1999) 2659–2666.
[20] M. Nishida, Phys. Rev. B 58 (1998) 7103–7112.
[21] D.A. Muller, P.E. Batson, J. Silcox, Phys. Rev. B 58 (1998) 11970–11981.
[22] (a) J. Cerda, A. Yoon, M.A. van Hove, P. Sautet, M. Salmeron, G.A. Somorjai, Phys. Rev. B 56 (1997) 15900–15918;
(b) J. Cerda, M.A. van Hove, P. Sautet, M. Salmeron, Surf. Sci. 409 (1998) 145–153;
(c) M.-L. Bocquet, J. Cerda, P. Sautet, Phys. Rev. B 59 (1999) 15437–15445.
[23] E. Canadell, M.H. Whangbo, Inorg. Chem. 25 (1985) 1488–1491.